SMALL AND LARGE SCALE MAGNETIC STRUCTURES INVOLVED IN THE DEVELOPMENT OF THE 1992 OCTOBER 28 SOLAR FLARE

N. Vilmer[1], J.P. Raulin[2], G. Trottet[1], N. Nitta[3], A.V.R. Silva [2], P. Kaufmann [2], E. Correia [2], A. Magun [4]

[1]DASOP, CNRS-URA 8046, Observatoire de Paris, F-92195 Meudon, France
[2]CRAAE/CRAAM, Instituto Presbiteriano Mackenzie, Rua da Consolação 896, 01302-907, São Paulo, Brazil
[3] Lockheed Martin Solar & Astrophysics Laboratory, Dep/L9-41, Palo Alto, CA 94304, USA
[4] Institute of Applied Physics, University of Bern, CH-3012 Bern, Switzerland

ABSTRACT

In this contribution, we present spatially resolved observations of the 1992 October 28 solar flare which were obtained in a wide range of wavelengths from soft and hard X-rays to millimeter and decimeter-meter radio wavelengths. This unique combination of data allows to investigate the magnetic structures at different spatial scales involved in the flare development, the localization of particle acceleration and the evolution with time of the number of accelerated electrons.

Key words: Sun: activity; Sun: flares.

1. INTRODUCTION

The 1992 October 28 Hα 1F flare occurred in NOAA region 7321 (S34W38) and was associated with a GOES C2.6 flare starting at 10:05:30 UT. The impulsive flare lasted until 10:12 UT and was observed from the HXR domain (up to 200 keV) to the dekametric radio domain. The present study does not deal with the post-impulsive radio emission (type II and moving type IV bursts) not associated with radio millimetric and HXR emissions. A more complete analysis of the event can be found in Raulin et al. (1999).

2. INSTRUMENTATION

The imaging HXR and SXR observations are obtained by the Hard X-ray Telescope (HXT) and the Soft X-ray Telescope (SXT) aboard YOHKOH. Images were obtained in quiet or flare mode with different field of views and pixel resolution varying between 2.46″ and 9.81″. SXT observed AR7321 in the quiet mode until 10:07:35 UT and in the flare mode after 10:09:07 UT. HXT has a total FOV of 35′ x 35′ and can detect HXR emission from the whole disk. Images can be produced in the 14-93 keV energy range in four energy bands with a spatial resolution of 5″ over a FOV of 2.1′ x 2.1′ (Kosugi et al. 1991).

HXR spectral data are taken from the Hard X-ray Spectrometer (HXS) aboard YOHKOH. It provides 32 channel spectra in the 24-830 keV range with a time resolution of 1s (Yoshimori et al. 1991). The values of the photon spectra deduced from HXS are checked to be consistent with HXT observations.

The millimeter observations are obtained at 48 GHz by the 13.7 meter dish of the Itapetinga observatory with a time resolution of 1ms and a sensitivity of 0.04 sfu. The multiple receiver focal array produces five beams of half power widths of 2′ which partially overlap (Georges et al. 1989). The observations of three of these beams are available here. This allows to localize the centroid positions of the emission at 48 GHz for some time interval during the flare (see Giménez de Castro et al 1999). Total flux measurements at 3.1 and 5.2 GHz from Bern are used to complement the observations.

The decimetric-metric radio imaging observations are obtained from the Nançay Radioheliograph (NRH) (The Nancay Radioheliograph Group 1993). In 1992, the data consisted of EW and NS 1D images of the solar brightness at 5 frequencies (164, 236.6, 327, 408 and 435 MHz). The time resolution is 1s and the spatial resolution for that event is at 164 MHz 1.4′ in the EW direction and 4.4′ in the NS direction. The spatial resolution is inversely proportional to the observing frequency. Radio dynamic spectra from Potsdam are used for spectral identification (Aurass, private communication).

3. OBSERVATIONS

3.1. Temporal Evolution of the Flare

The event has been divided into three time intervals (P1, P2,P3) on the basis of the time profile of the HXR flux above 100 keV (Figure 1) :

P1 : 10:07-10:0845 UT

Proceedings 8th SOHO Workshop 'Plasma Dynamics and Diagnostics in the Solar Transition Region and Corona', Paris, France, 22-25 June 1999, (ESA SP-446, October 1999)

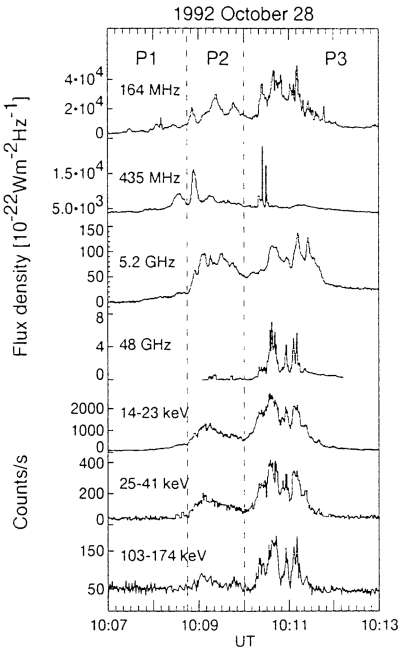

Figure 1. Temporal evolution of the 1992 October 28 flare observed at different wavelengths. From top to bottom: radio flux density observed at 164 and 435 MHz by the NRH, at 5.2 GHz by the Bern polarimeters and at 48 GHz by the Itapetinga telescope; X-ray count rates measured in the low energy channel of Yohkoh/HXT and in two energy bands of Yohkoh/WBS. The vertical dashed lines show the starting time of P1, P2 and P3.

It is characterized by a slow rise of the 14-23 keV X-ray emission, of the metric and the 5.2 GHz radio emissions. There is a low frequency cut-off of the metric/decimetric continuum and bursts around 150 MHz. No significant 48 GHz and HXR emission $\geq$ 25 keV are detected.

P2 : 10:08:45-10:10 UT

There is a sudden increase of HXR emission up to 170 keV and of the 3.1-5.2 GHz flux. A faint 48 GHz emission is detected from 10:09:12 UT and there is a shift of the low frequency cut-off of the metric-decimetric emission below 100 MHz.

P3 : 10:10-10:11:40 UT

The HXR emission is multiplied by a factor around 2 at all energies and the 48 GHz emission is multiplied by 10.

Figure 1 shows that energetic electrons are produced and interact in the upper and lower corona during the whole event. Electrons have access to lower density magnetic structures during P2 and P3 than during P1 (shift of the low frequency cut-off).

	P2	P3
e^- above 20 keV	$3.0\ 10^{36}$	$7.2\ 10^{36}$
e^- above 60 keV	$1.2\ 10^{34}$	$2.0\ 10^{34}$
ε in $e^- > 20$ keV (ergs)	$1.4\ 10^{29}$	$3.6\ 10^{29}$
ε in $e^- > 60$ keV (ergs)	$1.4\ 10^{27}$	$3.6\ 10^{27}$

Table 1. Number of electrons above 20 keV (60 keV) and corresponding energies, derived from the spectral analysis of HXS data.

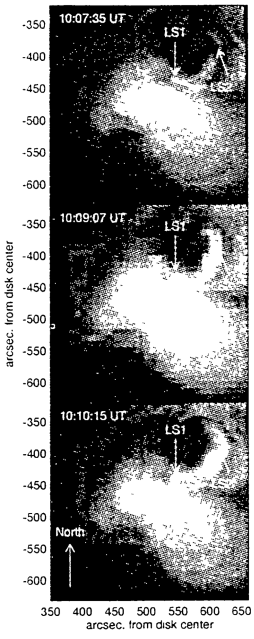

Figure 2. SXT (Al.1 filter) images of AR 7321. The arrows show the region LS1 and indicate the extension of the region LS2.

P1,P2 and P3 correspond to 3 successive episodes of acceleration with increasing efficiency for the production of non thermal electrons (see the X-ray time profiles in Fig. 1 and Table 1).

During P2 and P3, the HXR photon spectrum is well represented by a double power law with $E_b \simeq 60$ keV. $\gamma_1 \approx 2.9 \pm 0.3$ for $E \leq E_b$ for the whole event and γ_2 (above E_b) about 5.0 ± 0.5 (during P2) and 4.1 ± 0.2 (during P3).

3.2. SXR imaging observations

SXR emission (Figure 2) comes from a bright region at the centre of the images as well as from LS1 and LS2 :

* the bright SXT emission at the centre overlies the

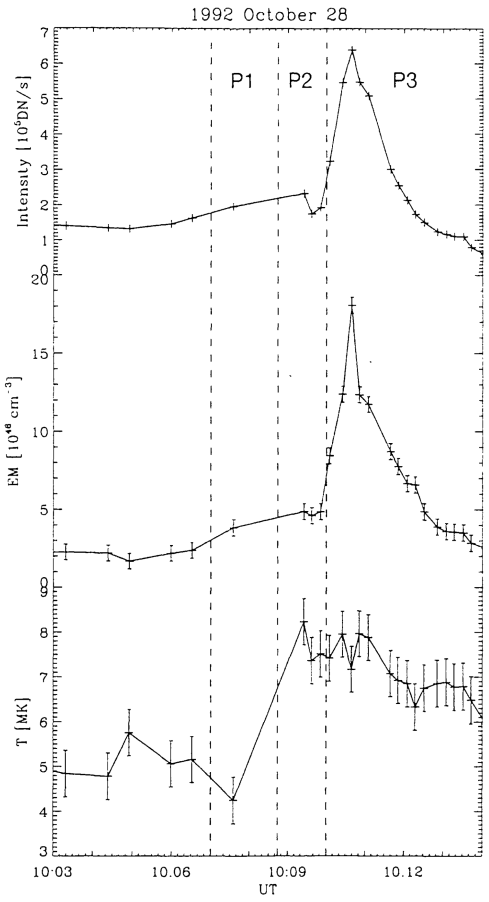

Figure 3. From top to bottom: temporal evolution of the SXR intensity (Al.1 filter), of the emission measure (EM) and of the temperature (T) for LS1 region.

main magnetic inversion line. SXR emission in this region varies smoothly during the flare and increases from 10:07 UT until 10:14:20 UT. While the temperature T remains constant at $\simeq$ 8 MK, the emission measure EM rises from 4.5 10^{47} cm^{-3} to 6 10^{47} cm^{-3}

* LS1 is over a short magnetic inversion line at the border of AR7321. It appears as a compact (20″) system of loops which starts to brighten at the onset of P1 (Figure 3). During P1 and P2, T increases from 5.5 MK to 7.5 MK and EM increases from 2.5 10^{46} cm^{-3} to 5 10^{46} cm^{-3}. During P3, T $\simeq$ 7.5 MK and EM reaches 1.8 10^{47} cm^{-3}. The thermal energy contained in LS1 at 10:10:40 UT is $W_{th} \simeq 2.5\ 10^{29}$ ergs.

* LS2 has a loop-like shape elongated in the SE-NW direction (100″). The NW part of LS2 brightens at the onset of P2. The brightening expands towards SE and reaches the SE extremity at the beginning of P3. (EM and T cannot be analysed for LS2 since it is outside of the smallest field of view of SXT).

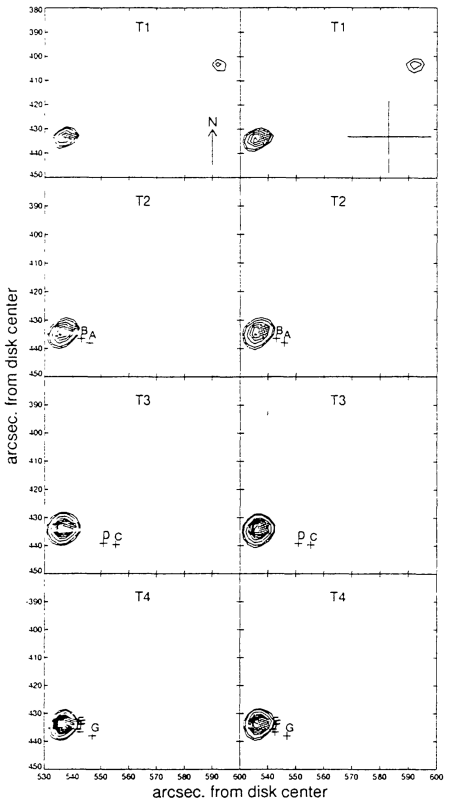

Figure 4. Contours of equal intensity of the HXR emission observed during T1-T4, in the 53-93 keV (left column) and 33-53 keV (right column) channels. Contour levels are 0.15, 0.2, 0.3, 0.4, 0.5, 0.6, 0.7, 0.8, 0.9 and 0.99 of the maximum emission detected during time periods T1 to T4. The grey filled contours show the HXR emission observed during the phase P2 (T0). The crosses A-G show the position of the 48 GHz radio pulses observed during T2, T3 and T4. The small (big) cross sizes represent the accuracy of the relative (absolute) position of the radio pulses A-G.

3.3. HXR imaging and 48 GHz observations

HXR images can be performed during P2 and P3 in the 53- 93 keV and 33-53 keV ranges (Figure 4). The brightest HXR emission comes from a compact (10″) not resolved loop system spatially associated with LS1. At the beginning of P3 a faint HXR source appears at the NW extremity of LS2.

The centroid positions of the bursts at 48 GHz (computed on 100 ms) are shown with cross symbols (relative accuracy 1.5″, absolute position 15″). As shown on Figure 4, the emission at 48 GHz and in the HXR range arises from the same loop system (LS1). However, no 48 GHz emission is seen at the NW part of LS2 (this is probably due to a weaker magnetic field at this extremity). Figures 4 and 5 also show that the different bursts at 48 GHz are observed at different positions during T2, T3 and T4.

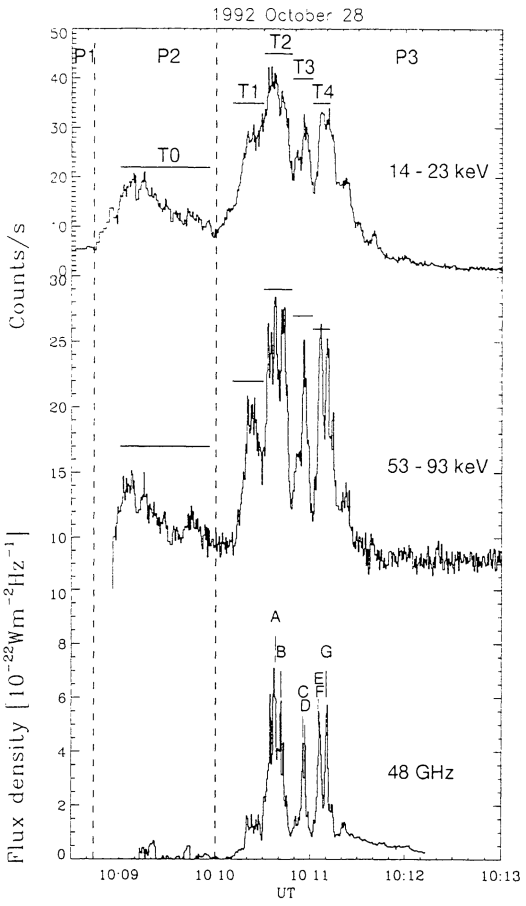

Figure 5. Expanded view of the temporal evolution of the HXR emission count rate (14-23 keV and 53-93 keV) and of the radio flux density at 48 GHz. Thick horizontal bars show time intervals (T0-T4) during which HXR contour maps have been computed. The letters A-G in the 48 GHz time profile note different temporal fast structures.

3.4. Spatially Resolved Metric/Decimetric Observations

In contrast to the HXR emission which shows a single compact source, the decimetric/metric emission comes from many sources (labelled A1-A8; B1-B7; C1-C10; D1-D7) (Figure 6). New emitting sources switch on during P1, P2 and P3 but no clear correspondence is observed between the time of appearance and duration of these sources and the transition between P1 to P2 and P2 to P3. The most striking feature is the organisation of the general spatial pattern of the radio emission (Figure 7) from 450 MHz to 164 MHz. It has a similar orientation as the one of the complex SXR emission connecting the flaring site in AR 7321 to a remote active region (AR 7316). The radio emission is probably generated in a large scale system of loops interconnecting both regions. The complex spatial distribution and the variations with

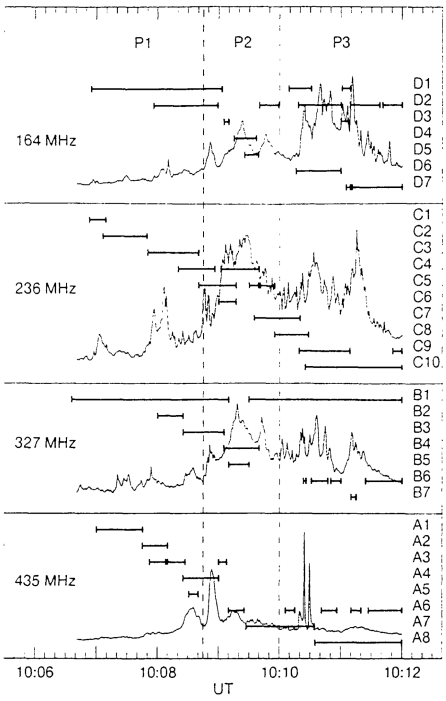

Figure 6. Time of appearance and duration of decimeter-meter radio sources observed at different locations at each NRH observing frequency (thick horizontal lines), superimposed on the flux density time profile

time indicate that the loop system is highly inhomogeneous and that electron trajectories change from one burst to the other in this complex of magnetic structures.

4. DISCUSSION

The three successive episodes of electron acceleration (P1,P2.P3) which correspond to stepwise increases of the electron non-thermal energy content switch on together with sudden changes of the X-ray brightness of flaring structures :

* The initial energy release occurs in LS1.

* The second episode of energy release starts with the brightening of the NW extremity of LS2 and with the increase of temperature as well as production of HXR in LS1. This may indicate some interaction between LS1 and LS2 loop systems. The brightening of the NW extremity of LS2 moves afterwards from the NW to the SE part of LS2 at a speed close to 500 kms^{-1} (close to a heat conduction front speed).

* The last episode of energy release coincides with the arrival at LS1 of the perturbation initiated at the NW extremity of LS2 at the onset of P2. The intense brightening of LS1 during P3 is the response of the

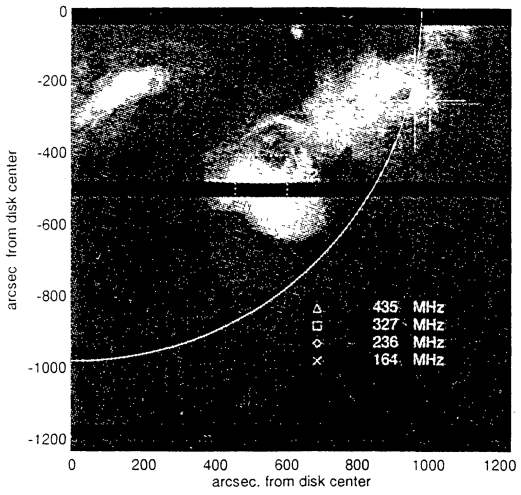

Figure 7. Decimeter-meter burst positions during P1, P2 and P3, superimposed on a SXR image taken at 10:07:25 UT. The crosses show the EW and NS extensions of the region covered by the ensemble of emitting sources observed at each NRH frequency. Dotted boxes show, from bottom to top, the position of optical active regions, AR 7321 and AR 7316. The small cross shows the location of the LS1 loop system.

loop system to a new energy input which can produce e.g. an increase of the electron density in LS1 due to chromospheric evaporation. Such an hypothesis is supported by the observation that the thermal energy contained in LS1 at 10:10:40 UT is comparable to the energy deposited by the accelerated electrons at the same time.

The spatial resolution of the X-ray imagers is not sufficient to resolve the small scales where magnetic reconnection and energy conversion takes place. The analysis of the spatial and temporal evolution of radio emissions provide additional tools to investigate these small scale processes :

* The very close similarity of the HXR and millimeter wave time profiles indicates a common origin of emitting electrons. Although positions of the sources at 48 GHz vary from one elementary burst to the other, the HXR emission remains almost spatially constant. This suggests that the loop system LS1 is inhomogeneous and that electron propagation paths within LS1 rapidly change from one burst to the other. This probably reflects changes (on time scales less than a second) of the location of the acceleration site within the energy release volume.

* Electrons radiating decimetric/metric emissions probably originate from the same accelerator as HXR and mm-wave emitting electrons (similarity of the global HXR and radio time profiles). The large number of radio emitting sources and their spread in positions show that many high coronal structures are involved in the propagation at large scales of the energetic electrons produced close to LS1. Electrons are injected successively along different large scale loops within the large complex of magnetic structures connecting the flaring site to a remote active region.

In summary, the spatially resolved radio observations support the idea that electron acceleration occurs at discrete sites, the locations of which vary on time scales of the order of a second in the primary energy release volume.

5. CONCLUSION

The 1992 October 28 flare is a relatively moderate one in terms of the amount of energy contained in both the thermal plasma (C2.6 GOES event) and the non-thermal electrons (a few 10^{29} ergs). Still, the magnetic structures involved in the flare development are complex at all spatial scales. Stepwise temporal evolutions of the amount of energy release and of the efficiency of non-thermal electron production are related to similar stepwise variations of the magnetic structures at different scales illuminated by hot plasma or by non-thermal electrons. The following conclusions were drawn in Raulin et al (1999):

On the scale of the global loop structures revealed by soft X- ray emission, the present observations support flare scenarios based on loop-loop interactions (see also Hanaoka 1997 and references therein).

At the smaller scales where magnetic reconnection, energy dissipation and particle acceleration take place, radio observations provide indirect support to the idea that these processes are highly fragmented in space and time.

In conclusion, this analysis provides some pieces of information to study how the small scale processes leading to particle acceleration are incorporated in the large scale coronal structures associated with the flaring region. This is one of the critical issues for understanding particle acceleration and building a realistic acceleration model.

REFERENCES

Giménez de Castro C.G., Raulin J.-P., Makhmutov V.S., Kaufmann P., Costa J.E.R, 1999, A&A (in press)

Georges C.B., Schaal R., Costa J.E.R., Kaufmann P., Magun A., 1989, in: SBMO-International Microwave Symposium/Brazil IEEE catalog No 89th0260-0, Vol. II, 447

Hanaoka Y., 1997, Sol. Phys. 173, 319

Kosugi T., Makishima K., Murakami T., Sakao T., Dotani T., Inda M., Kai K., Masuda S., Nakajima H., Ogawara Y., Sawa M., Shibasaki K., 1991, Sol. Phys. 136, 17

Raulin J.P., Vilmer N., Trottet G., Nitta N., Silva A.V.R., Kaufmann P., Correia E., Magun A., 1999, A&A (submitted)

The Radioheliograph Group 1993, Adv. Space Res. 13, 9, 411

Yoshimori M., Okudaira K., Hirasima Y., et al., 1991, Sol. Phys. 136, 347